FISEVIER

Contents lists available at ScienceDirect

## **Biosystems Engineering**

journal homepage: www.elsevier.com/locate/issn/15375110



## Research Paper

# Intensity-modulated optical fibre strain sensor for continuous measurements of below-the-surface food deformation during drying

Hamed Jafarishad <sup>a</sup>, Mucheng Li <sup>a</sup>, Yao Shen <sup>a</sup>, Pawan Singh Takhar <sup>b</sup>, Yuxiang Liu <sup>a,\*</sup>

- <sup>a</sup> Department of Mechanical Engineering, Worcester Polytechnic Institute, Worcester, MA, 01609, USA
- <sup>b</sup> Department of Food Science and Human Nutrition, University of Illinois at Urbana-Champaign, Champaign, IL, 61801, USA

#### ARTICLE INFO

#### Keywords: Large food deformation Continuous in-line measurements Fibre food sensor Computer vision

#### ABSTRACT

Measurements of food deformation during drying processes are important for food quality control but remain challenging. A mm-scale optical fibre strain sensor is presented here to address this challenge. The sensor can be embedded in soft foods to provide continuous and distributed measurements of large food deformation below the surface during drying. The sensor performance was investigated by both analytical and numerical models as well as the experimental calibration. To demonstrate its application in foods, multiple sensors were embedded inside fresh banana slices during a 4-h-long air-drying process for spatially distributed deformation measurements, during which the banana wet basis moisture contents dropped from around 80%–40%. The sensor measurements covered the full range of the banana normal strain from 0 to 20% and revealed the shell-hardening characteristics by providing both the spatial and time dependences of deformation. The faithfulness of the fibre sensor measurements was verified by measuring the banana surface deformation using computer vision. To the best of the authors' knowledge, this is the first senor in the literature that can measure the real-time deformation below the surface of food samples during drying. The presented fibre optical strain sensor has a high potential to contribute to improving both fundamental understanding and process monitoring of food drying processes.

## 1. Introduction

Foods deform when dried. The deformation is induced by the moisture loss from and movement in the food matrix, among other complex physical and chemical changes (Mahiuddin, Khan, Kumar, Rahman, & Karim, 2018). Food deformation is related to food quality parameters such as the texture, moisture content, crust formation, wholesomeness, and crack formation (Akiyama, Liu, & Hayakawa, 1997), all of which evolve during the drying process (Krokida & Maroulis, 2000). Knowledge of continuously changing food deformation is important both to enhance fundamental understanding and to improve the control of the drying processes. However, the intrinsic characteristics of foods and the process environments vary vastly, and it remains challenging to measure the deformation during drying, even for some common foods. The following are some of the challenges. 1) Food deformation sensors should measure a large deformation range. The deformation range of food can be reach 30%-70% over the whole drying process (Gulati & Datta, 2015). 2) The sensors should provide spatially distributed deformation measurements in real time during the food manufacturing processes. Space-wise, due to the complex structures of food matrices,

food deformation can be non-uniform, anisotropic, and heavily depends on the location of measurements. Time-wise, food deformation is not constant over time, and real-time knowledge of the deformation at the end of the drying process, when the deformation is the largest and the measurements are most difficult, is especially important for making a decision when to stop the drying. 3) The implementation of sensors in food samples is challenging. Before drying, some foods are soft while others have high moisture contents. It is difficult to create a flat, dry, and stiff surface for sensor attachment, so the conventional and widely used thin-film strain gauges are not a feasible solution. During the drying process, the large food deformation can also cause the sensor implementation to fail over time. Further, the implemented sensors could distort the local food deformation, resulting in the measurements different from the native food deformation. This issue of sensing faithfulness is especially of concern for soft food products such as banana slices. 5) The drying ovens and the harsh process environments often introduce additional concerns on the compatibility of the sensors.

Existing tools for deformation measurements in engineering can be categorised into contact-based and non-contact-based methods, and these methods rely on electrical sensing devices or cameras. The most commonly used contact-based method is the thin-film resistive strain

<sup>\*</sup> Corresponding author.

E-mail address: yliu11@wpi.edu (Y. Liu).

Nomenclature		$V_n$	Noise of photodetector output voltage (V)
		$\Delta L$	Changes of L (mm)
CV	Computer Vision	$\Delta P$	Change of pressure (Pa)
EM	Electromagnetic	$\Delta T$	Change of temperature (K)
FEM	Finite Element Method	$\Delta V$	Change of photodetector output voltage (V)
Α	Cross-section area of the sensor cavity (mm <sup>2</sup> )	$\Delta\delta$	Changes of $\delta$ ( $\mu$ m)
$b_r$	Buffering ratio	$\Delta arepsilon$	Resolution of the sensor (%)
E	Young's modulus (MPa)	$\delta$	Fibre-disc distance (μm)
F	Force (N)	$\delta_0$	Initial fibre-disc distance (µm)
k	Stiffness (N/mm)	$\varepsilon$	Strain (%)
L	Length of the sensor (mm)	λ	Wavelength of the light (nm)
$L_0$	Initial buffer sleeve length (mm)	$\nu$	Poisson ratio
$P_0$	Initial air pressure (Pa)	$\omega_0$	Mode field radius of the light beam at the initial location
$P_d$	Detected collected power (μW)		(μm)
$P_t$	Total emitted power(µW)	ω	Mode field radius of the light beam at light-collection
$T_0$	Initial temperature (K)		location (µm)

gauge (Window, 1992), often simply called a strain gauge. A typical strain gauge is centimetre-long and composed of a conductive wire that is embedded in a plastic film in a zig-zag pattern of parallel lines (Higson, 1964). When the strain gauge is glued to the surface of a sample, the sample deformation changes the conductive wire's length and hence its electrical resistance, the latter of which is measured to obtain the deformation. Alternatively, piezoelectric strain sensors with a similar form factor have been reported for contact-based measurements (Montazerian, Rashidi, Milani, & Hoorfar, 2020). However, the abovementioned sensors have not been applied to foods, to the best of the authors' knowledge. The possible reasons of these sensors lacking applications in foods include 1) too stiff or too large sensor form factors, 2) susceptibility of electrical readouts to the interference of electromagnetic (EM) waves in the environment (Erik, Michael, & Anthony, 2011), 3) the requirements of a flat, smooth, and hard surface on the sample for sensor implementation. Non-contact methods such as cameras and image processing techniques (Yuan, Tan, Xu, Yuan, & Dong, 2019) have been used to measure food deformation during drying, such as bananas (Madiouli et al., 2011), apples (Sturm, Nunez Vega, & Hofacker, 2014), pears (Silva et al., 2016), and potatoes (Carrasco et al., 2015; Yadollahinia, Latifi, & Mahdavi, 2009). Although these imaging-based non-contact methods do not suffer from the challenges encountered by the contact-based methods, they can only measure deformation on the exposed surfaces of foods. Nevertheless, it is often challenging for these non-contact methods to obtain continuous and real-time deformation during drying, due to the harsh drying environments including the strong EM fields and high temperature that can endanger the electronics and cameras. Cameras installed outside have compromised image quality and distortion due to the air currents and airborne particles in the light path. In summary, current electrical sensors and camera-based imaging methods cannot satisfy the need of continuous, real-time deformation measurements in foods during drying.

As an alternative to electrical sensors, optical fibre strain sensors have great potential to enable the food deformation measurements in harsh environments. Optical fibres have been utilised for strain sensor development thanks to the low cost and simplicity of sensor structure (Montazerian et al., 2020). Despite their wide applications in other engineering areas, optical fibre strain sensors have not yet been applied in food measurements, not to mention in drying processes, to the best of authors' knowledge. The reasons of the lack of fibre sensor application in foods will be detailed in Section 2-1-Working principles.

It should be noted that mathematical models have been developed to evaluate food deformation theoretically (Mahiuddin et al., 2018; Takhar, 2014), both to circumvent the difficulties in the experimental measurements and to obtain more detailed information on deformation. These models have been applied to several types of foods, such as corn

kernels (Takhar, 2011; Takhar, Maier, Campanella, & Chen, 2011), strawberries and carrots (Ozturk & Takhar, 2020a, 2020b), apples (Yuan et al., 2019), and potatoes (Aprajeeta, Gopirajah, & Anandharamakrishnan, 2015). However, it is difficult for numerical models to account for all the details of the real-world food matrix, such as material inhomogeneity and anisotropy, raising concerns about the faithfulness of the calculated results. Hence, experimental deformation measurements are beneficial to verify the faithfulness of these models.

In this study, an intensity-modulated optical fibre strain sensor is presented for continuous, real-time, and distributed measurements of soft food deformation below the surface during drying. To the best of author's knowledge, this work is the first reported strain sensor in the literature for below-the-surface food deformation measurements during drying. This sensor can measure the strain inside food samples by measuring the optical intensity at the readout. It is immune to EM waves in drying chambers because there is no electrical conductor or signal in the sensor and because the frequency of the optical signal (>100~THz) is much higher that of environmental EM waves (~GHz). The intensitymodulated sensor mechanism has been chosen because of the simple design and fabrication process. With a small footprint and soft shell, this sensor can potentially be applied to a large variety of food samples with different sizes and softness. In addition to systematic investigation of the sensor performance, the sensor capability of continuous, in-situ strain measurements in fresh banana slices over an air-drying process is demonstrated. This sensor is not limited to foods but can be potentially employed to measure the large deformation of other challenging soft materials, such as pulp and paper, soil, and muscular and neural tissues.

#### 2. Design

## 2.1. Working principles

First, the term "strain," which will be used extensively in the rest of the paper, is clarified here. In the conventional engineering context, mechanical deformation of an object is quantified by strains, where normal strains and shear strains define the changes of size and shape, respectively. A normal strain is defined as the ratio of the length change to the initial length between two points that are fixed to and move with the object during its deformation. A positive normal strain corresponds to elongation and a negative strain to compression.

A brief review of fibre optical strain sensors in the literature is provided in the following, in order to lay a foundation for the sensor design of this work. A typical working principle of optical fibre strain sensors is to convert the sample deformation into the change of a sensing element on or next to the fibre, the latter of which is often a length or a position change and can be directly detected through the fibre. In this sense, most

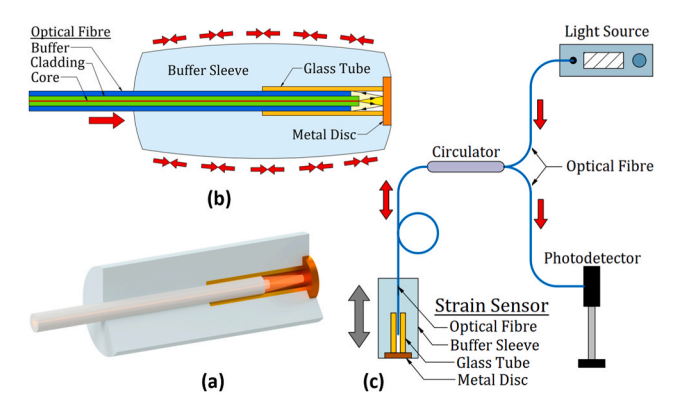


**Fig. 1.** Design of optical fibre strain sensor. A) 3D model and b) 2D schematic of the optical fibre strain sensor. C) Sensor readout system.

fibre strain sensors are essentially displacement sensors. Intensitymodulated strain sensors (Lagakos, Bucaro, & Jarzynski, 2010; Zheng & Albin, 1999), in which the readout is the optical intensity and is modulated by the external strain, are one of the most common fibre strain sensors (Lagakos et al., 2010). Various applications for the optical fibre strain sensors have been reported, including structural health monitoring of buildings and bridges (Deng & Cai, 2007; Merzbacher, Kersey, & Friebele, 1996), vehicle fatigue testing (Murphy, Gunther, Vengsarkar, & Claus, 1992), and damage detection (Liu, Wu, Rao, Jackson, & Fernando, 1998). The existing designs of fibre strain sensors cannot address the challenges posed by soft food materials during drying, detailed below. First, the abovementioned optical fibre strain sensors are much stiffer than soft foods, such as fruits and vegetables (Lagakos et al., 2010). Second, existing fibre strain sensors have limited measurable strain ranges. All the above fibre sensors can only measure strains up to 1%, far below the common strain range in foods. As a result, the current sensors cannot cover the large range of strains in foods. None of the existing fibre strain sensors has been applied to foods. Ideally, a fibre strain sensor should be small, soft, readily mountable inside food samples, and compatible with harsh environments such as strong EM waves.

In this paper, the aim is to develop a sensor to measure the normal strain along the sensor direction, which can be any desired direction in the food. It does not measure any shear strains. Therefore, the strain in the rest of the paper refers to the normal strain to avoid redundancy, unless stated otherwise. Moreover, only measuring the shrinkage of the food samples, where the normal strain should always be negative is desired. Therefore, the normal strain is described by its absolute value. For example, the aim is to measure a compressive food strain of 20%, without using -20% in the text.

The designed optical fibre strain sensor consists of a buffer sleeve, glass tube, metal disc, and optical fibre, all of which are depicted in Fig. 1(a). All the optical fibres in this work are single-mode (SMF-28, Corning Inc, Corning, New York) and the used optical wavelength is around 1300 nm. The fibre is inserted from the left end of the tube. At the right end, the glass tube is glued to a metal disc, serving as a mirror. When light is emitted from the fibre tip, the reflected light from the metal disc is collected by the same fibre, with the collected light power dependent on the fibre-disc distance due to the light divergence. The buffer sleeve is made of silicone softer than skin and is glued to the outer surface of glass tube and the optical fibre portion outside the tube. When mounted inside a food sample, the outer surface of the buffer sleeve is in direct physical contact with, and deforms together with, the food. When the sample deforms during drying, the deformation of the buffer sleeve leads to the slide of the fibre inside the glass tube (Fig. 1(b)), resulting in the fibre-disc distance change and hence the collected light power change, the monitoring of the latter of which allows the measurements of the food strain along the fibre direction. A schematic of the sensor

readout system is illustrated in Fig. 1(c). Light from a pigtailed benchtop super-luminescent diode (SLD, S5FC1021S, Thorlabs Inc, Newton, New Jersey) with a centre wavelength and bandwidth of 1310 nm and 85 nm, respectively, goes through the fibre circulator (CIR-3-1290-1620-L-10-FA-5.5  $\times$  38, Ascentta Inc, Somerset, New Jersey) and is emitted from the fibre tip in the sensor. The collected portion of the reflected light travels backward along the fibre, through the fibre circulator, and its power is measured by the photodetector (PDA20C, Thorlabs Inc, Newton, New Jersey). The output of the photodetector is a voltage proportional to the received optical power.

One of the main features in this design that differ from the other fibre strain sensors is the buffer sleeve. The functions of this buffer sleeve are fourfold. 1) It holds the fibre position inside the tube and prevents the fibre from slipping freely; 2) When the food deforms, the buffer sleeve moves the fibre inside the tube, changes the fibre-mirror distance, and modulates the optical intensity received by the optical fibre, allowing for reliable measurements of the food deformation. 3) The buffer sleeve is softer than human skin and small ( $\sim$ 1.2 mm in diameter) in size, minimising the influence on the food deformation when the food has similar or higher stiffness. 4) The buffering effect allows smaller strain inside the sleeve than the outside food, reducing the displacement of the fibre, which enables a large strain measurement range. To quantify the buffering effect, the buffering ratio,  $b_{r_0}$  is defined as

$$b_r = \frac{\Delta L}{\Delta \delta},\tag{1}$$

where L is the length of the food sample in contact with the outer surface of the sensor,  $\delta$  is the fibre-disc distance, and  $\Delta L$  and  $\Delta \delta$  are the changes of L and  $\delta$ , respectively. When the thickness of the buffer sleeve approaches zero,  $\Delta L$  approaches  $\Delta \delta$  and  $b_r$  approaches 1, indicating no buffering effect. The larger  $b_r$ , the higher the buffering effect, and the smaller the fibre-disc distance change compared with the food deformation.

## 2.2. Design parameters

To understand the role of the buffer sleeve and hence obtain a proper design, a finite element method (FEM) with commercial software (COMSOL Multiphysics 5.6, COMSOL Inc, Burlington, Massachusetts) was employed to simulate the sensor mechanical response to the deformed food on the outer sidewall. Two-dimensional simulation was performed on a single cross-section passing the axis of the sensor, with an axisymmetric model in COMSOL's Structural Mechanics module. The geometrical and material properties of the sensor used in the simulation are listed in Table 1. The dimensions of the sensor components were chosen to achieve the goal of decreasing the sensor footprint. A smaller sensor footprint reduces the averaging length of the strain measurements, enabling more localised strain measurements. The smallest sizes were limited by the fabrication process and the available tools used in the fabrication which are detailed in Section 3-1-Sensor fabrication. The FEM meshed model is shown in Fig. 2(a). As can be seen, the model was divided into several domains to be able to apply quadrilateral elements through mapping. This model included the optical fibre, glass tube, metal disc, and buffer sleeve, as shown in Fig. 2(b). The deformation of the food during drying is a slow process, so elastic behaviour of the

**Table 1**Geometrical and material properties of the designed sensor.

Geometrical Properties		Material Properties		
Sensor length	3.0 mm	Buffer sleeve, $E$	0.5 MPa	
Sensor diameter	1.2 mm	Buffer sleeve, $\nu$	0.48	
Optical fibre diameter	0.25 mm	Optical fibre	Rigid	
Glass tube length	1.5 mm	Glass tube	Rigid	
Glass tube diameter	0.36 mm	Metal disc	Rigid	
Metal disc diameter	0.6 mm			

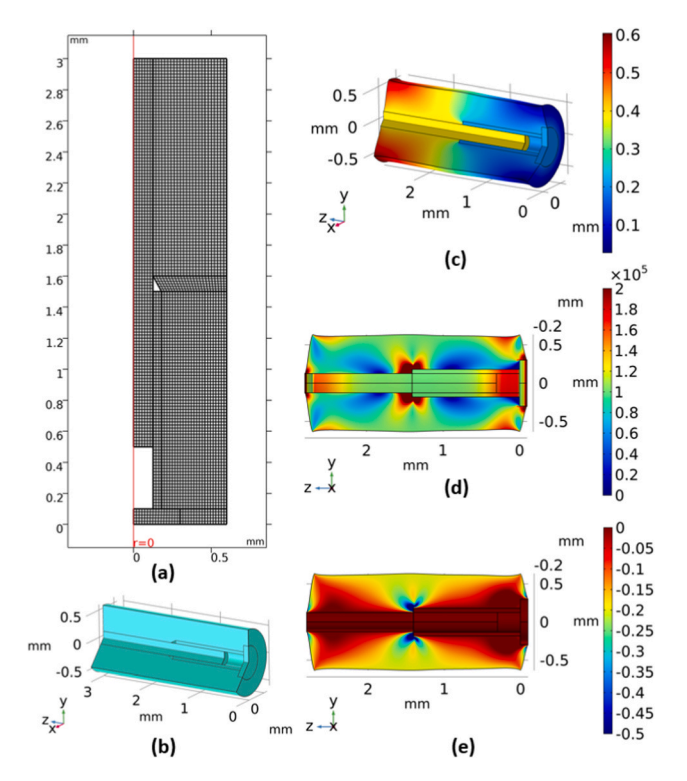


**Fig. 2.** a) Meshed model and b) 3D perspective view of the mechanical FEM model to simulate the sensor deformation. Simulation results of the distributions of the c) displacement, d) von Mises stress, and e) normal strain along the sensor axis, in response to a compressive 20% strain applied to the outer surface of the buffer sleeve.

buffer sleeve was assumed. The glass tube, optical fibre, and metal disc were all assumed to be rigid because they are much stiffer than the buffer sleeve. No sliding was considered on the contact surfaces between the inner sidewall of buffer sleeve and the fibre, between the inner sidewall of buffer sleeve and glass tube, or between the outer sidewall of buffer sleeve and the food sample. The sensor is assumed to be fully embedded inside the food sample and the physical contact between the food and sensor is on the cylindrical outer surface of the sleeve. By assuming a uniform food shrinkage on the contact surface, a uniform shear strain on the outer cylindrical surface of the buffer sleeve was applied in the direction of the sensor axis. The calculated sensor response is shown in Fig. 2(c), when there is a negative (compressive) 20% food strain applied on the outer surface of the buffer sleeve. A shrinkage of 0.6 mm occurs on the outer surface of buffer sleeve. By comparison, the change of the fibre-disc distance is about 0.2 mm, which, based on Eq. (1), results in a buffering ratio of  $\sim$ 3. The contour of von Mises stress, which is the stress equivalent to distortion, is presented in Fig. 2(d). The maximum stress in the buffer sleeve is about 200 kPa and occurs at three locations: the left and right ends of the sensor and the left end of glass tube, all three on the inner sidewall of the buffer sleeve. The high stress at the two ends of the sensor results from the large deformation mismatch between the outer and inner sidewall of the sleeve. The high stress at the left end of the glass tube indicates that the fibre slides into the tube, pinching the sleeve at this location, which might not really occur, given the difficulty in realising a conformal adhesion between the sleeve and the fibre or tube at this location. Nevertheless, the safety of the sleeve under these stresses is not a concern because the silicone rubber (sleeve material, detailed in Section 3-1-Sensor fabrication) has a tensile stress of 2.0 MPa. The contour of the normal strain along the axis of the sensor is shown in Fig. 2(e). The deformation is highest on the outer surface and keeps decreasing with the depths below it, except for the fibre entrance of the tube due to the abovementioned pinching effect.

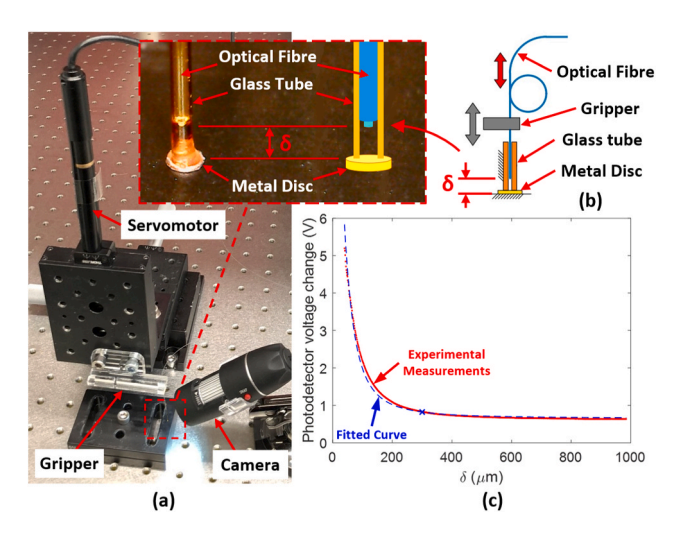


**Fig. 3.** Measurements of power of detected light versus the fibre-disc distance. a) Experimental setup. (Inset) closed-up of the fibre tip and disc. b) Schematic of the setup. c) Dependence of detected power on the fibre-disc distance  $(\delta)$ . The cross indicates the desired  $\delta$  used in the fabrication process, which was also the initial value in the calibration and measurements. Dots: experimental measurements; dashed line: fitted curve based on analytical model.

These simulation results confirmed the intended benefits of the buffering effect, which allows the measurements of high (20%) food strains with the fibre-tip distance change three times smaller than without the buffering layer. Such a scaledown is necessary because there is a higher boundary in the optically measurable fibre-disc distance. As the fibre tip goes too far away from the mirror, the reflected light is too weak to differentiate meaningful changes in distance. The thickness or the length of the buffer sleeve can be increased to obtain a higher buffering ratio and hence a higher measurable food strain range, at a cost of a larger sensor size. Although small, each strain sensor still occupies a finite volume in the food, so the measured strain essentially is averaged over the occupied volume. A larger sensor size will increase such an averaging effect, which is not desired considering the inhomogeneous nature of food deformation. Therefore, to determine a proper sleeve thickness in the sensor design, a further understanding of the measurable range of fibre-disc distance is needed. In other words, if a sensor with the design parameters in Table 1 is chosen to measure 20% compressive food strain, it should be confirmed that a 0.2 mm fibre-disc distance is practically measurable.

Such an experimental study was conducted with the setup shown in Fig. 3(a). A single-mode optical fibre (SMF-28, Corning Inc, Corning, New York) was fixed on a home-made gripper holder, which was in turn fixed on a translational motion stage. The optical fibre was inserted and readily slid inside the glass tube (1068150026, Molex LLC, Lisle, Illinois), which was fixed to the optical table with a copper disc glued at the tube bottom. The motion of the stage in the vertical direction was controlled by a servomotor (Z825B, Thorlabs Inc, Newton, New Jersey) to change the fibre height and hence the fibre-disc distance. The same readout system as in Fig. 1(c) was used, with the sensor replaced by the setup in Fig. 3(a), to characterise the dependence of optical power readout on the fibre-disc distance ( $\delta$ ). A schematic of the setup is illustrated in Fig. 3(b). As the servomotor moved the stage vertically, the distance between the fibre tip and copper disc changed which resulted in changes in the power of reflected light.

The obtained experimental results are plotted in Fig. 3(c). As the fibre tip got closer to the copper disc, the measured power increased exponentially. This increase results from the divergent nature of fibre-emitted light and can be well explained by the equations describing free-space optical propagation, detailed in the following. Since single-mode optical fibres were used throughout this work, the light emitted from the fibre tip was always a fundamental Gaussian mode, which has

the smallest beam waist at the tip surface and gradually increase the spot size with the propagation. After the light is emitted from the fibre, propagates to the disc, is reflected, and travels back to the fibre, the optical power that is collected and detected by the fibre can be described by (Siegman, 1986)

$$P_d = P_t \frac{1 - e^{-2(\omega/\omega_0)^{-2}}}{1 - e^{-2}},\tag{2}$$

where  $P_d$  and  $P_t$  are the detected collected and total emitted powers, respectively.  $\omega_0$  and  $\omega$  are the mode field radii of the light beam at the initial (the emission end face of the single-mode fibre) and light-collection (the same end face of fibre but after the light round trip) locations, respectively. In air,  $\omega$  is a function of fibre-disc distance ( $\delta$ ) and can be calculated as

$$\omega(2\delta) = \omega_0 \sqrt{1 + \left(\frac{2\delta\lambda}{\pi\omega_0^2}\right)^2},\tag{3}$$

where  $\lambda$  is the wavelength of the light. With Eqs. (2) and (3) combined and a consideration of fibre tip internal reflection added, the dependence of detected power on  $\delta$  can be written as

$$P_d = A \left( 1 - e^{-2 \left[ 1 + \left( \frac{2\delta \hat{a}}{2\pi u_0^2} \right)^2 \right]^{-1}} \right) + B, \tag{4}$$

where A is  $P_t/(1-e^{-2})$  and B is a constant added to account for the internal reflection at the fibre tip (it is not derived from Eqs. (2) and (3)), which results in a non-zero detected power in the experiment even if  $\delta$  approaches infinity. In practice, A and B are parameters to be determined experimentally. The values of  $\lambda$  and  $\omega_0$  in the experiments were 1.31  $\mu$ m and 4.6  $\mu$ m, respectively. As shown in Fig. 3(c), the experimental measurements can be well fitted by the theoretical model described by Eq. (4) with a  $R^2$  coefficient of determination of 0.987, and the fitting parameter values of A and B are 11.6 V and 0.659 V, respectively. Such a good fitting confirms the faithfulness of the theoretical model, supports the sensor design and the decisions on sensor parameters, and allows the conversion from the photodetector voltage readout to fibre-mirror distance change, the last of which will be used in the rest of the paper in both the sensor calibration and banana testing.

According to Fig. 3(c), there was a 460  $\mu m$  dynamic range of  $\delta$ , i.e., between 40 and 500  $\mu m$ , where  $\delta$  can be reliably measured based on the reflected optical power. This dynamic range is more than twice the  $\sim\!200~\mu m$  fibre-disc distance needed to achieve the goal of measuring 20% food strains according to the FEM model. In principle, the buffer sleeve thickness or length further could be decreased, resulting in a smaller sensor, without compromising the goal. However, it was decided to use the design in Table 1 for the rest of the paper as a proof of concept. This leaves a safety factor of about 2.3 in the measurable strain range to cover any factors that cannot be well controlled in the sensor fabrication and implementation. Therefore, the designed optical fibre strain sensor should be able to measure food strains up to and possibly higher than 20%.

In the following, more details are provided on how the  $\delta$  range of  $40{\sim}500~\mu m$  was determined from experimental results that are plotted in Fig. 3(c). On the lower end, as the fibre tip went too close to the mirror ( $\delta<40~\mu m$ ),  $\delta$  approached the coherence length ( $\sim\!20~\mu m$ ) of the light source, resulting in an interference pattern and a sinusoidal dependence of the intensity on  $\delta$  (data not shown). This dependence is not desired in the current intensity-modulated sensor design and should be avoided. Therefore, the data were not recorded when  $\delta<40~\mu m$ . On the higher end, there was no hard cut-off of the  $\delta$  range, so 500  $\mu m$  was chosen with certain ambiguity. For example, the distance could still be measured by the optical power at  $\delta\sim\!520~\mu m$ , given the low power fluctuation at a fixed  $\delta$ . It should be noted that the larger  $\delta$  will reduce the sensitivity and

resolution of the strain measurements, due to the smaller slope of power-  $\delta$  curve in Fig. 3(c). As will be seen later in Section 3-1-Sensor fabrication, the initial  $\delta$  value of 300  $\mu m$  was targeted in the sensor fabrication (marked as a cross in Fig. 3(c)), where the  $\delta$  range of  $50{\sim}300~\mu m$  was needed to cover the 20% compressive food strains with a purpose to avoid a higher  $\delta$  range and the corresponding low sensitivity and resolution, and to avoid a lower  $\delta$  range close to coherent length. If one needs to measure elongation rather than compression of the food sample, the initial  $\delta$  in the fabrication should be chosen to be closer to 40  $\mu m$ . In this case, the elongated food sample moves the fibre away from the mirror during drying, and the same sensor design and the calibration curve in Fig. 3(c)) will be able to cover 20% or more positive normal strain.

#### 3. Materials and Methods

#### 3.1. Sensor fabrication

The fabrication process of the sensor consisted of three phases, namely the fabrication of the buffer sleeve, fabrication of the reflective cap, and assembly. The process is detailed below in this section.

The fabrication started with Phase I, the fabrication of the buffer sleeve. A soft silicone rubber (Dragon Skin FX- Pro, Smooth-On, Macungie, Pennsylvania) was used as the buffer sleeve. This silicone rubber has a tensile strength of 2.0 MPa, which is considerably larger than the maximum stress calculated from the simulation and therefore should not rupture during measurements. At the first step, a cylindrical silicone rubber tube was fabricated with a moulding process, serving as the soft buffer sleeve outside the glass tube that will be detailed in the next paragraph. As shown in Fig. 4(a), a syringe needle (16 Gauge) with an inner diameter of 1.2 mm was filled with uncured, liquid silicon rubber to define the outer surface of the silicone cylinder. One benefit of using a syringe needle is the available and easy assembly of a syringe body with the needle, where the syringe body facilitates the pressure application on the liquid silicone during the moulding (Fig. 4(d)). A steel wire with a diameter of 0.25 mm was held inside the needle syringe to define a concentric thorough hole in the moulded rubber cylinder. The purpose of the hole was to house the optical fibre and glass tube later in the fabrication. Several small acrylic pieces were designed (Parts i, ii, and iii in Fig. 4(a-c)) to align and support the metal wire and the syringe needle, to ensure they were concentric. These acrylic pieces allowed the flow of uncured, liquid silicone rubber into the mould when pressed and avoid air trapping inside the mould. These custom pieces were fabricated by cutting commercial acrylic pieces (8560K172, McMaster-Carr, Elmhurst, Illinois) with a thickness of 1/16" each with a laser cutter

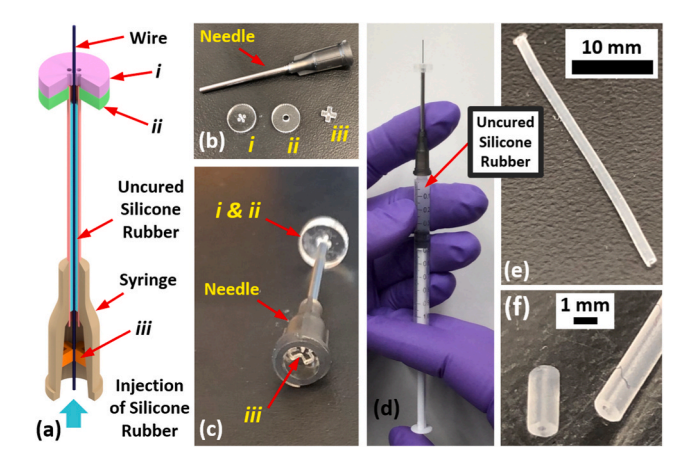


**Fig. 4.** Phase I of the fabrication process: fabrication of the buffer sleeve. a) Schematic of the moulding setup. b) Acrylic pieces and a syringe needle. c) Assembled pieces with a needle. d) Injection of the silicone rubber into the mould. e) Cured silicone rubber tube pulled out from the mould. f) A 3-mm-long silicone rubber tube cut from the long one.

(PLS6.150D, Universal Laser, Scottsdale, Arizona), followed by the assembly shown in Fig. 4(c). After the injection of the silicone rubber into the mould and cure of the rubber, the moulded rubber was pulled out from the mould (Fig. 4(e)) and was cut using a knife blade into 3-mmlong sections (Fig. 4(f)).

Phase II of the fabrication was to make the reflective cap, which was composed of a glass tube and a reflective copper disc fixed at one of the tube ends. The cap fabrication was carried out in three steps, as shown in Fig. 5(a). First, a copper disc with a diameter of 0.6 mm and thickness of 0.05 mm was cut by a syringe needle tip from a copper sheet. The flat end face of a commercial glass tube (1068150026, Molex LLC, Lisle, Illinois), which has outer and inner diameters of 360  $\mu m$  and 250  $\mu m$ , respectively, was pushed against the copper disc (Fig. 5(a) Step 1), followed by applying super glue around the tube-disc contact surface (Fig. 5(a) Step 2). The other end of the tube was cut using a capillary column cutter (Capillary GC Column Cutter, Restek, Bellefonte, Pennsylvania) to obtain a 1.5-mm-long cap (Fig. 5(a) Step 3) that allowed an optical fibre to slide in.

The final phase of the fabrication was the assembly of the buffer sleeve with the reflective end, as shown in Fig. 5(b). First, a single-mode optical fibre (SMF-28, Corning Inc, Corning, New York) tip was inserted into the 3-mm-long silicone rubber tube fabricated in Phase I. The fibre has an outer buffer layer made with acrylate, middle glass cladding, and centre glass core, with the diameters of 250  $\mu$ m, 125  $\mu$ m, and 8.2  $\mu$ m, respectively. The fibre can freely slide inside the silicon rubber tube and in the glass tube. The tube was slid along the fibre far away from the fibre tip, so it was not shown in Fig. 5(b) until it was slid back to the tip in Step 3. The fibre tip was then inserted into the glass tube (Fig. 5(b) Step 1). The fibre-disc distance was adjusted and simultaneously measured by using the method described in Section 2-2-Design parameters and results in Fig. 3(c), until the desired value of  $\delta \sim 300 \ \mu m$  was achieved. As discussed at the end of Section 2-2-Design parameters, an initial  $\delta = 300 \ \mu m$  was chosen in the fabrication, resulting in an expected  $\delta$  range of 100~300  $\mu m$  when the food shrinks by 20%, to prove the concept of the sensor while retaining a high sensitivity and resolution. Note that  $\delta$  is supposed to decrease after the sensor is mounted in foods that shrink in the drying process. A bead of liquid silicone glue (Sil-Poxy, Smooth-On, Inc, Macungie, Pennsylvania), which was different from the silicone rubber used before, was gently applied to the part of the optical fibre that was outside the glass tube (Fig. 5(b) Step 2). Finally, the silicone rubber tube was slid down along the fibre to fully cover the glass tube, distributing the silicone glue and fixing the sleeve inner sidewall with the tube and fibre (Fig. 5(b) Step 3). The curing of the glue took 12 min at room temperature (20 °C), completing the sensor fabrication process. A typical fabricated optical fibre strain sensor is shown in Fig. 5

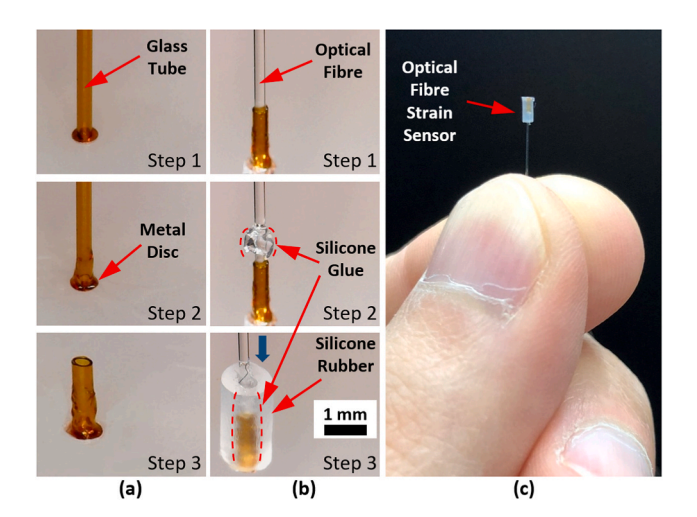


**Fig. 5.** Phases a) II and b) III of the sensor fabrication process. c) Fabricated optical fibre strain sensor.

(c). If a larger measurement range of food strains is needed, a shorter sleeve can be readily cut to enable a higher buffering ratio, without any changes of the other components or the fabrication procedure.

#### 3.2. Sensor calibration

The sensor performance is characterised by obtaining the dependence of the sensor readout on the strain of the sample in which the sensor was embedded. The calibration setup, shown in Fig. 6(a), allows a well-controlled strain to be applied to the sensor. A transparent silicone rubber cylinder was moulded to mimic a food sample, as shown in Fig. 6 (c). In the rubber cylinder, there were a central through hole and four off-axis through holes that were equally spaced from the centre and along 4 orthogonal directions. The purpose of the centre through hole was to house the sensor, and that of the other four holes was to prevent the bucking of the cylinder under compression. Two translational stages controlled by servomotors (Z825B, Thorlabs Inc, Newton, New Jersey) were used to compress the two ends of the silicone cylinder and to control its strain, as shown in Fig. 6(b) and(d). A (Microscope-1000x, Bysameyee, Amazon.com, Seattle, Washington) camera was used to monitor the sensor during the embedment and the calibration processes, thanks for the transparency of the cylinder. The sensor embedment process is depicted by the schematics in Fig. 6(e) and the corresponding photos Fig. 6(f). First, a steel tube with inner and outer diameters of 1.6 mm and 2.1 mm, respectively, was pushed through the central hole from the right, until it reached the other end face of the cylinder. Since the inner diameter of steel tube was larger than the sensor outer diameter, the sensor was readily inserted into the steel tube from the left until it reached the middle of the cylinder. The steel tube was pulled out from the right, leaving the sensor embedded along the cylinder axis and at the centre of the cylinder both in axial and radial directions.

This setup was used to calibrate four replicas of the sensors. Each sensor was calibrated in three loading-unloading cycles, providing measurements of 12 loading-unloading cycles in total. In each cycle, the cylinder was initially undeformed, gradually compressed by the two servomotors until 20% compressive strain was obtained, and gradually released. The servomotor positions and the sensor readouts were recorded in the whole process. After each cycle, the cylinder and sensor were left to rest for at least half an hour before the next cycle. The calibration curves were obtained by the dependence of the cylinder strain on the optical readout from the sensor. The cylinder strain at the sensor location was considered to be equal to the spatially averaged axial compressive strain in the whole cylinder, the latter of which was obtained by the ratio of the cylinder length change to the initial length. The cylinder length change was obtained by the movements of the servomotors, which were set by the authors. It was assumed that the compressive strain in the axial direction was uniform in the silicone cylinder, because of the homogeneous and isotropic mechanical properties of the silicone, the rotationally symmetric geometry of the cylinder, and the axial compressive loading on two large flat end faces of the cylinder.

A theoretical model was needed to describe the experimentally measured calibration data. By considering Eq. (3), the strain on the outer surface of the sensor buffer sleeve, which is equal to the silicone cylinder strain at the sensor location, can be expressed as

$$\varepsilon = \frac{\Delta L}{L_0} = \frac{\Delta L}{\Delta \delta} \frac{\Delta \delta}{L_0} = b_r \frac{\Delta \delta}{L_0} = b_r \frac{\delta - \delta_0}{L_0},\tag{5}$$

where  $\delta_0$  and  $L_0$  are the initial fibre-disc distance and initial buffer sleeve length, respectively, before loading.  $\delta_0$  and  $L_0$  were set to be  $\sim 300~\mu m$  and 3 mm, respectively, in the fabrication process. For a fabricated sensor,  $b_r$  is fixed, so  $\varepsilon$  changes linearly with  $\delta$ . With Eqs. (4) and (5) in consideration, the dependence of the change of measured photodetector voltage, which is proportional to the collected optical power, on the cylinder strain can be described as

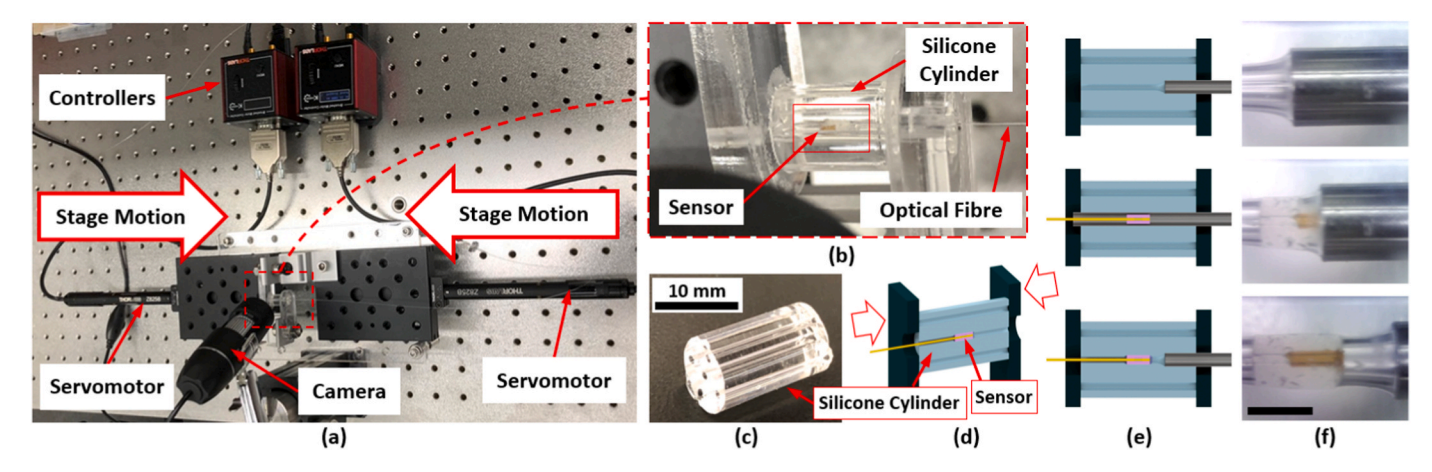


**Fig. 6.** a) Calibration setup and b) a close-up. c) Transparent silicone rubber cylinder to mimic the food. d) Schematic of the cylinder between stages with the sensor inside. e) Schematics and f) photos to depict the steps of inserting the sensor inside the cylinder (top to bottom). Scale bar in (f) = 2 mm.

$$\Delta V = -A \left( e^{\frac{-2}{1 + (Ce + D)^2}} - e^{\frac{-2}{1 + D^2}} \right), \tag{6}$$

where  $\Delta V$  is the change of photodetector readout voltage, A is 11.6 V determined in Section 2-2-Design parameters,  $C=2\lambda L_0/\pi\omega_0^2b_r$ , and  $D=2\lambda\delta_0/\pi\omega_0^2$ . In practice, both C and D are constants to be determined by the fitting to the experimental data. The second term on the right-hand side of Eq. (6) is to allow for the vanishing of voltage change at zero strain. It is noted that, in Eq. (6), compressive strain was experienced both by the silicone cylinder and by the fibre sensor.

#### 3.3. Sensor demonstration in drying

After conducting the calibration to evaluate the sensor performance, the application of the optical fibre strain sensors was further demonstrated in foods by continuous measurements of the shrinkage below the surface of fresh banana slices during drying. Fresh banana was chosen because it is a common fruit readily available across the world. It is challenging to measure under-surface strains of banana slices with conventional methods, due to the soft texture, high moisture content, non-uniform and large deformations during drying, and large mechanical stiffness changes during drying. Therefore, fresh banana slices make a good example of foods to demonstrate the capability of the optical fibre strain sensors.

The experimental setup is presented in Fig. 7(a). Cavendish bananas with a Brix value between 20% and 25% were purchased from local food markets and peeled. They, around the middle part, were cut into slices, each with a thickness of ~7 mm and a diameter of ~30 mm. The banana slice was placed near the centre of an oven (Large 13 Quart Glass Air Fryer, NutriChef, Philadelphia, Pennsylvania). The oven was slighted modified by the authors to accommodate the need of the experiment. The electrical heating coil, which is a resistance wire, was relocated from the top to the bottom of the oven, and the original cover and fan on the oven top were replaced with a transparent ~4.5-mm-thick flat acrylic cover. A camera (OT-HD, Opti-Tekscope LLC, Amazon.com, Seattle, Washington) was mounted above the oven to image the foods inside the oven through the acrylic cover. Drying of the banana slices was conducted for 4 h at 80 °C, which is an optimal temperature for banana drying (Macedo, Wallaf, Cintia, Sérgio, & Luciano, 2020). There was no fan inside the oven and the air currents were a result of gravitational convection. A thermocouple (TL1004 K-Type, PerfectPrime, London, England) was placed next to the banana slice inside the oven and was connected to the electrical power source for the feedback control of temperature, as shown in Fig. 7(b). The wet basis moisture contents of the banana slices were 80  $\pm$  2% before and 40  $\pm$  5% after the drying. As depicted in Fig. 7(c), the fibre strain sensor was inserted into a hole created from the banana slice sidewall along the radial direction,

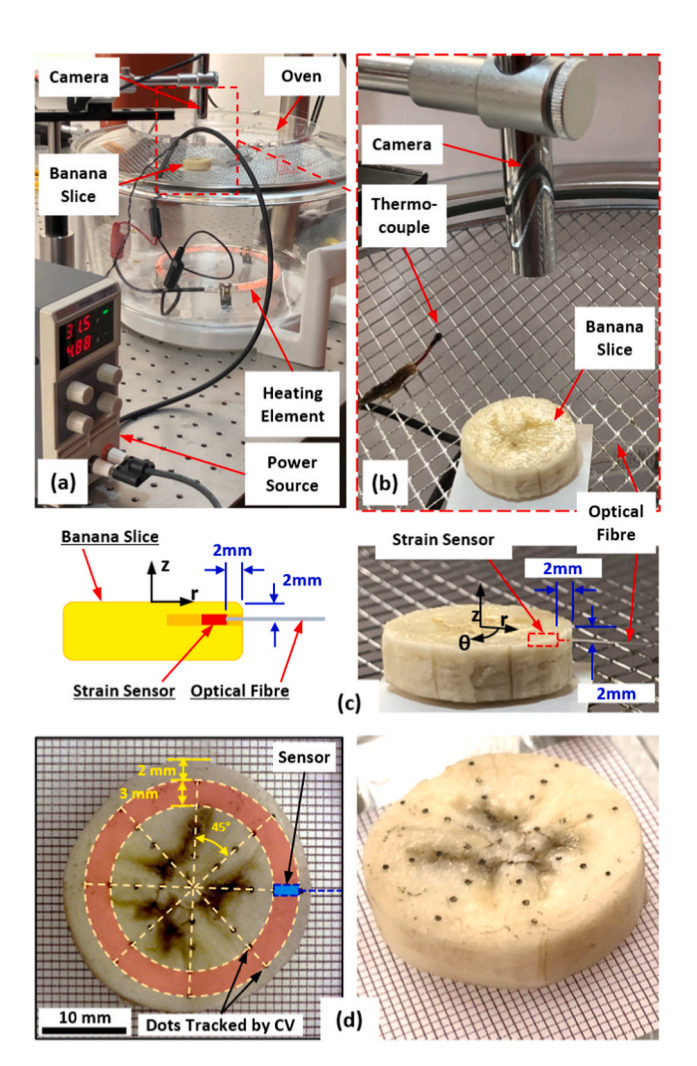


**Fig. 7.** Sensor demonstration in the drying of fresh banana slices. a) Drying setup. b) Close-up. c) (top) Schematic and (bottom) photo of a banana slice with the sensor embedded. d) Sample preparation with ink dots marked on the banana slice top surface.

about 2 mm below the top surface. Thus, the fibre sensor provided the measurements of the compressive normal strains in the radial direction of the banana slice at the sensor location. Note that the radial direction was chosen to demonstrate the sensor measurements without specific

reasons. The fibre sensor can be inserted in any desired direction into the food sample and will be able to provide the normal strain measurements along that direction.

Due to the banana softness and wet surfaces, which are challenges of any strain sensor implementation, some details of the fibre sensor implementation to ensure a good contact and grip between the banana and sensor are provided here. The hole in banana was created with a metal tube with an outer diameter of 1 mm which is slightly smaller than sensor diameter (1.2 mm), resulting in the banana gently squeezing on the outer surface of the embedded sensor. The tight fit helped to achieve a uniform contact between the banana and the cylindrical outer surface of the sensor and hence a reliable sensor attachment inside the banana. To implement the sensor in a banana slice, the fibre end of the buffer sleeve was held, and the fibre sensor was pushed into the hole by hand, without using any additional starch or glue between the banana and sensor. There was enough amount of starch in the fresh banana that provided gradually enhanced grip on the fibre sensor during the drying. That said, the grip might not be the most reliable in the beginning of the drying process, where the banana deformation was small and less important, but the grip was better and sensor readout more reliable toward the drying end, where the deformation was large and the measurements more crucial.

The fibre sensor tests were repeated with a total of four sensors and 14 banana slices having the same thickness cut from the same banana finger. A different banana slice was used in each test with one fibre sensor embedded at the same radius and depth in the slice. Each sensor was reused for 3 or 4 tests until the sensor surface got contaminated and performance degraded. To reuse the sensors, they were removed by soaking the dried banana slices in water and softening them. It was recognised that the banana mechanical properties along the azimuthal direction have non-uniform distributions, which was difficult to observe before the sensor insertion. Therefore, a random radial direction of each banana slice was chosen to insert the sensor along, and an average strain obtained from all the sensor measurements in the 14 slices, to remove the azimuthal dependence. The final expected results are the time-dependent strain continuously measured by the fibre sensors at a fixed radial position on all 14 banana slices over the whole drying process.

A computer vision (CV) method was used to analyse the camera images as an alternative measurement approach of strains on the top surfaces of banana slices, serving as a comparison and validation for the fibre strain sensor measurements. To facilitate the CV measurements, 32 ink dots were marked, before drying, along eight radii (dashed straight lines) on the top surface of each banana slice, with an angle of 45° between each adjacent radii, as shown in Fig. 7(d). The highlighted ring indicates the area at which the CV-based measurements were carried out. The inner and outer radii of the highlighted ring coincide with 8 pairs of 2 dots that were used for the strain measurement. 2 dots of each pair were at the same radial location of the ends of the embedded fibre strain sensor that is shown in Fig. 7(d). Along each radius, 4 dots were marked that were ~3 mm apart from each other, with the outermost dots ~2 mm away from the circular edge. Four banana slices, cut from the same banana fingers as those used for fibre sensor tests, were dried for CV measurements. These four slices did not have fibre sensors embedded in order to avoid the influence of embedded fibre sensors on the banana deformation.

## 4. Results and Discussion

## 4.1. Calibration results and sensor performance

The calibration results are shown in Fig. 8. With a sensor embedded in a food-mimicking cylinder, as shown in Fig. 8(a), the sensor deforms together with the cylinder. When the compressive strain of the cylinder was 0%, 10%, and 20%, the fibre-disc distance ( $\delta$ ) became smaller in turn, as can be seen in Fig. 8(b). The statistical calibration results of 12 measurements from four sensors are plotted in Fig. 8(c). It can be seen

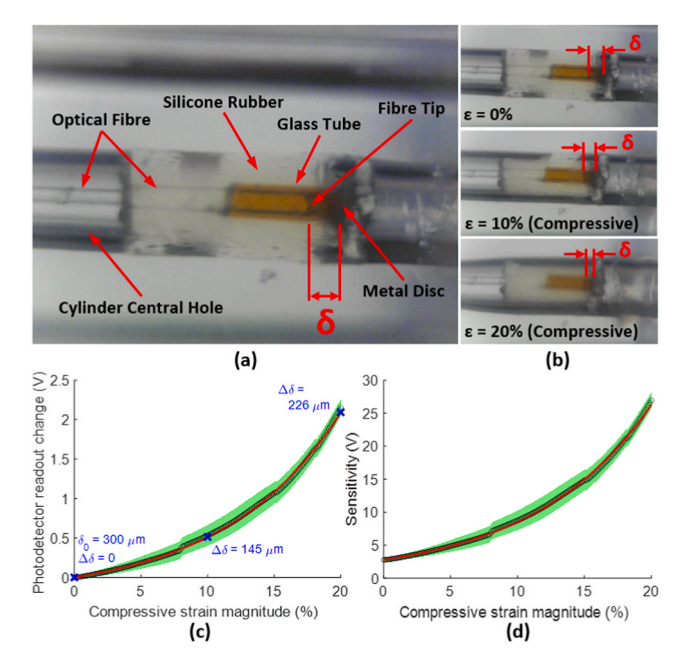


Fig. 8. Calibration results obtained through 12 measurements from 4 different fibre strain sensors. a) Photo of a sensor embedded inside the food-mimicking silicone cylinder. b) Photos of sensor responses to different cylinder strains. c) Cylinder strain versus the photodetector readout change. Three points on the curve were labelled by crosses, corresponding to the three photos in (b). The three labelled  $\Delta \delta$  values are calculated by combining the measured photodetector readout changes and the results in Fig. 3(c) d) Sensitivity of the sensor, which is the derivate of photodetector readout with respect to strain, versus the strain. Since the strain is dimensionless, the unit of the sensitivity is the same as that of the photodetector output (V). In (c) and (d), circles: experimental measurements; solid lines: fitted curves; hatched area: uncertainties of measurements.

that the sensors were able to measure the cylinder compressive strain up to 20%, confirming the validity of the sensor design. As explained in Section 2-2-Design parameters, the strain rose exponentially and monotonically with the collected optical power in the experimental measurements. The uncertainty at each compressive strain magnitude was obtained from the standard deviations calculated from all 12 measurements. The sources of the uncertainties include the differences in the performances of the four fibre sensors resulting from the different fabrication processes, different implementation processes, position control repeatability of the servomotors, repeatability of the mechanical responses of the cylinder in the loading-unloading cycles, and noise of the light source and the photodetectors. The small standard deviations throughout the 0-20% strain range indicate that the moulding-based fabrication renders a good repeatability and a good controllability of the sensor performance, promising a high potential for automatic and batch fabrication processes. Eq. (6) was used to fit the experimental calibration data, with the fitted curve plotted in Fig. 8(c). A fitting was obtained with a  $R^2$  of 0.999, with fitting parameters C = 0.183 and D =6.225. This good fitting indicates that the theoretical model of Eq. (6) closely describes and predicts the sensor performance. Note that the data in Fig. 8(c) are the most important results of the calibration. With these data, one can embed the sensor in any food sample and measure unknown food strains based on the photodetector readout of the sensor.

Before discussing the sensor demonstration in real foods, a few commonly used sensor characteristics and the buffering ratio will be discussed, the last of which is specific to this sensor, to understand the performance of the strain sensor.

**Dynamic range.** The dynamic range describes the range of the desired parameter that can be reliably measured. The dynamic range of the fibre strain sensor is  $0\sim20\%$  compressive strain. According to Figs. 3

(c) and Fig. 8(c), the dynamic range corresponding to 50  $\mu m < \delta < 300$   $\mu m$ . Note that a strain higher than 20% was not realised in the experiment, because the silicone cylinder started to buckle. Therefore, the sensor was not tested under the sample strain higher than 20%, and it is possible that the higher boundary of the dynamic range is greater than 20%.

**Sensitivity.** Sensitivity is another important characteristic of sensors and is defined as the derivative of sensor readout with respect to the input. In the fibre strain sensor, the input and readout are the strain to be measured and photodetector voltage change, respectively. The sensitivity is essentially the slope of the experimentally measured curve in Fig. 8(c). The dependence of sensitivity on the strain is plotted in Fig. 8 (d). The sensitivity depends on the cylinder strain. The sensor is more sensitive as the cylinder deforms more, which is expected because  $\delta$  is smaller and the working condition of the sensor is closer to the left-hand side of the curve in Fig. 3(c). Such a strain-dependence of the sensitivity is particularly beneficial in food drying, because the sensor provides more sensitive strain measurements at the later stage of drying, in which stage the strain information is more important to make a proper decision on stopping the process.

**Resolution.** Resolution of the sensor can be calculated as  $\Delta \varepsilon = V_n / v_n$ Sensitivity, where  $V_n$  is the noise in voltage in the photodetector readout of the sensor. In the fibre strain sensor, the sensor noise could be caused by three sources: the light source noise, photodetector noise, and mechanical drifts between or instability of different sensor components. All the three the noise sources are manifested as the fluctuations of photodetector readout, when the embedded fibre sensor is deformed by the silicone cylinder and held in place. In principle, such fluctuations depend monotonically on the sensor signal which in turn depends on the silicone cylinder strain. In practice, due to the difficulty to quantify such fluctuations at every possible cylinder strain, such fluctuations experimentally were measured to be 0.010 V, 0.014 V, and 0.020 V at the cylinder strains of 0, 10%, and 20%, respectively. Therefore, the photodetector noise was overestimated over the whole cylinder strain range of 0~20% to be 0.020 V. In particular, in the  $\delta$  range of 900~1000  $\mu m$  in Fig. 3(c), where light reflection from the mirror can be neglected and the last noise source vanished, the photodetector voltage fluctuation was found to be  $\sim 0.002$  V, significantly smaller than 0.020 V. This fact validates the noise estimation of 0.020 V because only two of the noise sources, namely light source noise and photodetector noise, existed and the sensor signal was smaller in this range than the that in the sensor dynamic range. Because sensitivity is not constant, the resolution depends on the strain. The highest and lowest resolutions of the sensor were ~0.08% and 0.72% in absolute value of normal strain, occurring at the strains of 20% and 0, respectively.

**Buffering ratio**  $b_r$ . Using the dependence of photodetector voltage change on  $\delta$  plotted in Fig. 3(c), the voltage can be converted in Fig. 8(c) to  $\delta$ , which is plotted as the solid curve in Fig. 9(a), and in turn find  $\Delta \delta$  by  $\delta - \delta_0$ . Since  $\Delta L$  can be readily calculated by  $\varepsilon \bullet L_0$ , which is plotted as the diagonal dashed line in Fig. 9(a),  $b_r$  can be determined, by  $\Delta L/\Delta \delta$ following Eq. (1), at any strain from the measured calibration data. The obtained  $b_r$  is plotted as the solid curve in Fig. 9(b). Note that the experimental buffering ratio is always less than 3, i.e., less than the value expected from the FEM simulation in Section 2-2-Design parameters. The discrepancy between the buffering ratios from the simulation and experiment might result from the imperfect binding between the buffer sleeve and the fibre or the glass tube, which most likely occurred at the fibre entrance of the glass tube. The geometry of the entrance of glass tube imposed a challenge on the conformability of the buffer sleeve step coverage, especially after the fibre was moved into and out of the tube caused by the sensor deformation. Such a challenge might lead to the delamination of the buffer sleeve from the local fibre or glass tube, while this delaminated portion of buffer sleeve did not function to scale down the deformation on the fibre-disc distance, leading to a smaller  $b_r$ . In general, a partial binding with the buffer sleeve anywhere along the fibre or glass tube could lower the buffering ratio which was observed in

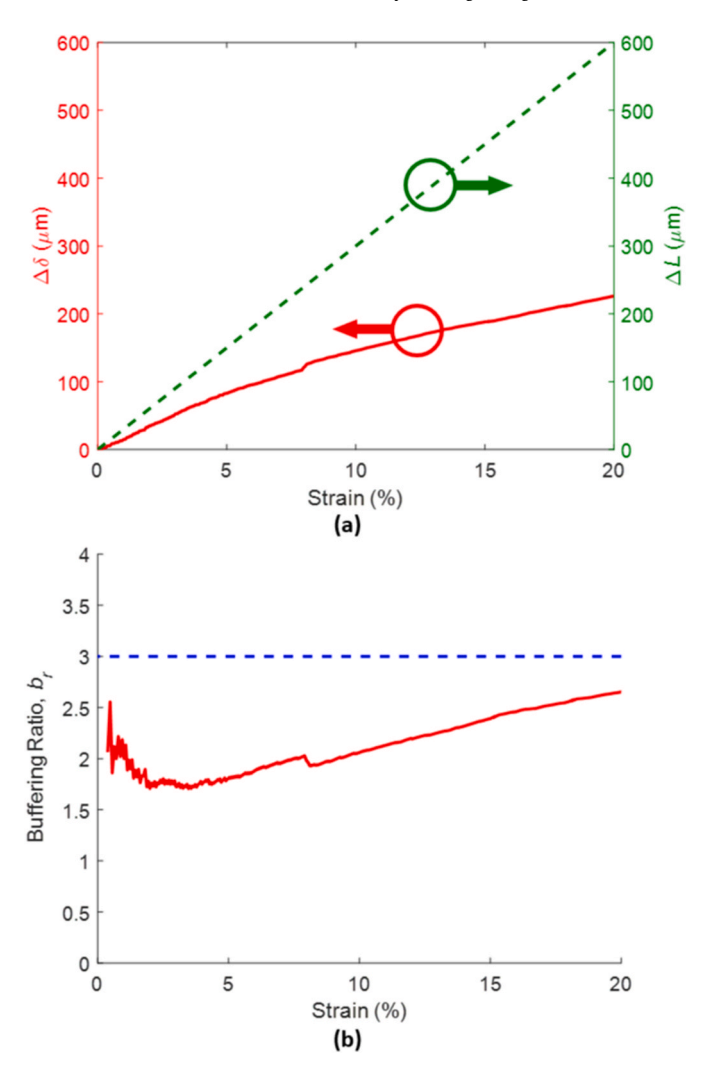


**Fig. 9.** Evaluation of the buffering ratio from the experimental calibration results. a) Dependence of the length change on the outer sidewall of buffer sleeve ( $\Delta L$ , dashed line) and the fibre tip displacement ( $\Delta \delta$ , solid curve) on the cylinder strain. Solid line: fibre tip displacement; dashed lines: change of buffer sleeve length. b) Buffering ratio ( $b_r = \Delta L/\Delta \delta$ ) at different cylinder strains. Solid line: experimental measurements; dashed line: simulation results.

the experiments.

## 4.2. Drying test results

In this section, first, the CV measurements are discussed. Then, the fibre strain sensor measurements are discussed and compared with the CV measurements. As the banana slice was dried and shrank, these dots moved accordingly, as shown in Fig. 10, were continuously tracked by the camera images during drying, and their position changes were analysed by the image-processing after drying to calculate the strain between each two adjacent dots. To remove the azimuthal dependency of the strains in each slice, the strains measured by all the outermost dot pairs in 8 radial directions were averaged to obtain the CV-measured strain in this slice, for the purpose of comparison with the fibre sensor measurements. Therefore, the final CV measurements of the time-dependent strain at the fibre sensor radial location were obtained by averaging those obtained from all 4 banana slices at any given time in the drying process.

It is worth noting that the CV measurements were limited on the banana slice surface, while the fibre strain sensors measured strains 2 mm below the surface, so a perfect match between the measurements of

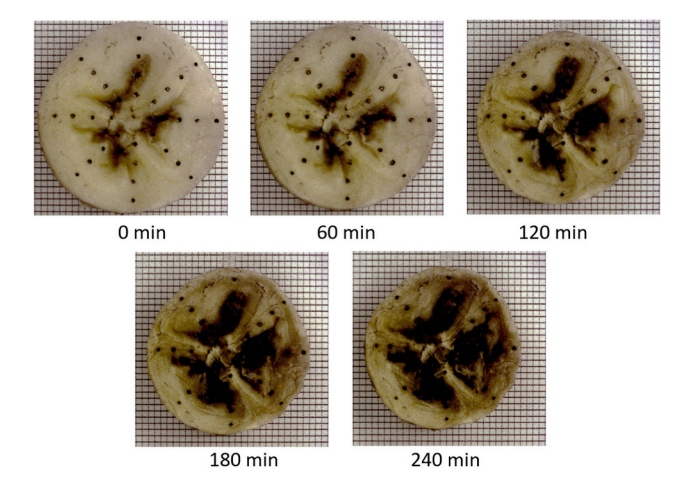


**Fig. 10.** Computer vision (CV) based surface strain measurements. Photos of the banana slice taken at different times in the drying process. All the photos share the same magnification and viewing angle.

CV and the fibre sensor is not expected due to the location difference. Since there is no existing method to measure strains below the banana surface, which is why this fibre strain sensor is unique and beneficial, CV measurements still provided a reference to validate the developed fibre strain sensors.

The change of photodetector readout of the fibre strain sensors during the whole drying process is shown in Fig. 11(a). As the banana shrank, the measured voltage increased, indicating a reduction in the fibre-disc distance ( $\delta$ ) Using the model described in Eq. (6), the photodetector readout change at any time point in Fig. 11(a) was converted to banana. The resulting fibre sensor strain measurements, as well as the CV measurements, of the banana slice are shown in Fig. 11(b). There is a good agreement between these two measurements, and the discrepancy in between reveals interesting information of the banana slice drying. First, the CV measured strains are higher throughout the drying, with a strain difference of 2~5% except in the first 10 min. The larger CV measurements are expected because the air-drying process removes the moisture more efficiently from the surface than internal, resulting in the surface deformation always larger than internal deformation. Such a difference between surface and internal behaviour is also referred to as the shell-hardening effects (Ozturk & Singh Takhar, 2020). Time dependence-wise, the slope of the CV measurements was highest in the beginning, gradually reduced in the first 50 min, and stays less changed in the rest of the drying process. This indicates that the surface drying and hence, the surface deformation was fastest in the beginning due to the high initial moisture content, slowed down due to the reduced moisture contents and enhanced difficulty of moisture removal, and finally became stable when most of the removed moisture came from the food volume through the surface. By comparison, the fibre sensor measured strain started very slow before 40 min, rose fast from 40 to 90 min to reach to the strain measured through CV, and stays stable and almost always parallel to the CV measurements after ~90 min with the discrepancy of ~2% strain. This result confirms that the air-drying started from the surface and that the moisture removal from below the food surface, as well as the resulting deformation, occurred with a time delay. The comparison between the time dependence of the two measurements indicates that the moisture removal from the banana surface was dominant in the first 40-50 min of drying, after which time the dominant drying effect was to remove the moisture below the surface. The effective moisture removal at 2 mm below the surface, where the fibre sensor was embedded, ended at  $\sim$ 90 min. It is hypothesised that the effective removal of the moisture after 90 min occurred deeper in the food matrix, and the study of the depth dependence of the strain is part of the continuing research. The above discussion implies that the fibre optical strain sensor, by providing previous unavailable information in

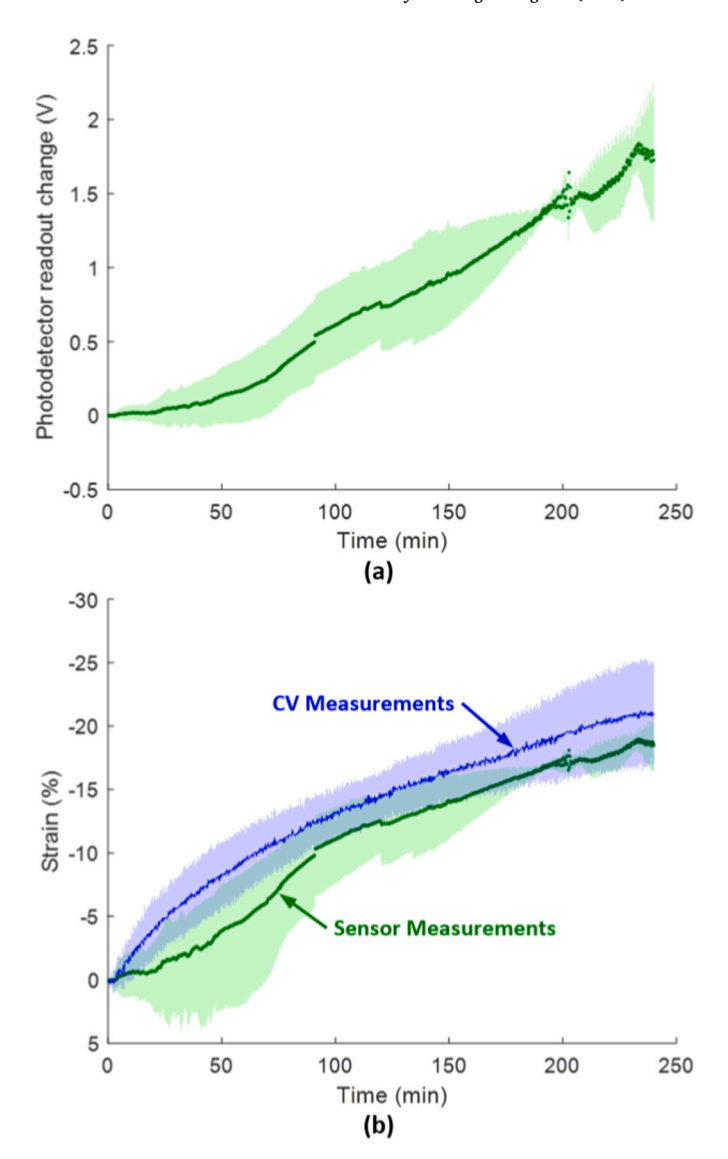


Fig. 11. Optical fibre strain sensor and Computer vision (CV) measurements. a) Experimentally measured signal from 14 tests obtained from four optical fibre strain sensors. Dots: experimental measurements; hatched area: standard deviation. b) Calculated strain from optical fibre strain sensor signal by using calibration data and CV measurements. CV measurements were done on four banana slices where 8 strains were measured from each slice (32 strain measurements in total). Dots: sensor measurements; hatched area: standard deviation of sensor measurements; solid line: CV measurements; hatched area: standard deviation of CV measurements.

food study, has a high potential to provide new understandings of the food drying process.

The strain of the banana slice in Fig. 11(b) reached  $\sim$ 20%, as measured by both the CV and fibre sensor, proving that the fibre sensor design goal of measuring 20% food strains was achieved. As discussed in Section 2-2-Design parameters, the design parameters, including the geometrical and material properties of the components, can be readily changed to obtain a higher buffering ratio, further extending the measurable strain range. For example, a higher buffering ratio can be obtained by increasing the thickness, decreasing the length of the buffer sleeve, or choosing softer silicone rubbers to fabricate the buffer sleeve.

The optical signal from the sensor might be influenced by environment temperature changes which would compromise the faithfulness of strain measurements. Therefore, the understanding of the temperature influences on the sensor readout is worthwhile to estimate the temperature influence. In the presented fibre strain sensor, temperature

changes can deform the sensor and influence the sensor readout by varying the thermal expansion of the solid parts of the sensor and by changing the air pressure inside the sensor. Considering both effects, the FEM simulation and analytical model showed that strain caused by a temperature change of 60 °C (from 20 °C to 80 °C) is  $\sim\!0.52\%$  (Appendix A). This temperature-induced sensor deformation is not from food samples, creating an artificial signal. However, such a temperature influence is much smaller than the real strain range of the food ( $\sim\!20\%$ ). Additionally, it should be noted in the fibre sensor, the strain is measured based on the change of fibre-disc distance rather than the absolute position of the fibre or the disc.

#### 5. Conclusion

An optical fibre strain sensor is presented for the measurement of food deformation during drying. To the best of authors' knowledge, this work demonstrates the first reported strain sensor that enables continuous deformation measurements below the food surface and the first reported one that is mechanically flexible enough to be embedded in soft food samples, in the present study, fresh banana slices, with minimal changes to the natural food deformation. The small sensor footprint allowed the measurements of deformation at a mm-scale location in a food sample. One of the key design features of this fibre sensor is the soft buffer sleeve on the sensor outer surface, which enabled a large measurable deformation range while minimising the sensor influence on the native food deformation. The fibre sensor can be embedded inside food samples without the need of any adhesive, because the soft sensor surface and the starch existing in the food matrix help to prevent sensor sliding inside the food. The buffer sleeve was fabricated by a moulding process, which resulted in highly repeatable sensor performances. The rest of the fabrication and assembly processes were straightforward without requiring any specialty facilities. To obtain a systematic understanding of the sensor performance, the sensor characteristic attributes were experimentally determined using four replicate sensors, including sensor responses to external strains, dynamic ranges (0-20%),

sensitivity (3-27 V), and resolution (0.08-0.72%). Moreover, the fibre strain sensors were applied to continuously measure the deformation below the surfaces of fresh banana slices during a 4-h-long drying process, to demonstrate the capability and faithfulness of the sensor for challenging food samples. The banana slices were wet and soft in the beginning and were dry with glassy textures at the end, with a wet basis moisture content of around 80% and 40%, respectively. A good agreement was obtained between measurements by the optical fibre strain sensors and by the computer vision (CV) method with a discrepancy of ~2% strain, proving the faithfulness of the fibre strain sensor measurements. The discrepancies between the results of the two methods reveal the differences between the surface and below-the-surface strains. Specifically, both the spatial and time dependences of the measured strains showed characteristics of shell-hardening effects. The sensor tests in the banana slice drying demonstrate the fibre strain sensor capability of continuous, in-situ, and below-the-surface strain measurements and indicate that such an unprecedented sensor has a high potential to contribute to improving both fundamental understandings and process monitoring of food drying processes.

#### **Declaration of Competing Interest**

The authors declare that they have no known competing financial interests or personal relationships that could have appeared to influence the work reported in this paper.

#### Acknowledgments

This study was partially supported by the US Department of Energy (# DE-FOA-0001980), the Center for Advanced Research in Drying (CARD), and the Massachusetts Clean Energy Center (MassCEC). CARD is a US National Science Foundation Industry University Cooperative Research Center. CARD is located at Worcester Polytechnic Institute, with the University of Illinois at Urbana-Champaign as the co-site.

#### Appendix A. Temperature influence on strain measurements

Temperature changes can influence the fibre strain sensor in two ways: 1) by thermally expanding the solid parts of the sensor and 2) by increasing the pressure of the air trapped inside the sensor cavity (the space between the fibre and the disc). To study the thermal expansion of the solid parts, the same FEM model described in the main text (Section 2-2-Design parameters) was used, with a few modifications to be detailed next. The physical module of thermal expansion was added in the FEM software to the sensor model. The applied external strain to the sensor outer layer, which was used 2-2-Design parameters, was replaced with a zero-displacement constraint along the sensor axis. The zero-displacement constraint was applied based on the assumptions that the sensor adhere perfectly to the food sample without delamination and that the sensor thermal expansion cannot deform the food. The second of the above assumptions is true when the sensor thermal expansion is small, or the sensor buffer sleeve is much softer than the food in contact with the sensor.

Sensor artifacts due to thermal expansion. The thermal expansion coefficients considered for the silicone rubber buffer sleeve and glass parts, the latter of which include the glass tube and optical fibre, are  $3 \times 10^{-4}$  °C°-1 and  $5 \times 10^{-7}$  °C°-1, respectively. The contour of displacement caused by the thermal expansion of the sensor under the temperature increase of 60 °C is calculated and shown in Fig. A.1. The calculated increase in fibre-disc distance is 3.8  $\mu$ m. Considering the buffering ratio  $b_r = 3$  and the buffer sleeve length  $L_0 = 3$  mm for the strain sensor, this increase in fibre-disc distance is equivalent to 0.38% strain.

Sensor artifacts due to air pressure increase. To study the increase of air pressure inside the sensor, it was assumed that the air trapped between the fibre and the disc, i.e., in the sensor cavity, is a perfect gas. Therefore, under the assumption of small changes, the dependence of air pressure on the volume and temperature can be described as

$$\frac{\Delta P}{P_0} + \frac{A\Delta\delta}{A\delta_0} = \frac{\Delta T}{T_0},\tag{A.1}$$

where  $P_0 = 1.013 \times 10^{-5}$  Pa and  $T_0 = 293$  K are the initial pressure and temperature inside the sensor cavity before drying, respectively, A the cross-section area of the sensor cavity,  $\Delta P$  the change in the air pressure, and  $\Delta T$  the change in the temperature. Because the initial fibre-disc distance ( $\delta_0 = 300 \, \mu \text{m}$ ) is one-tenth of the buffer sleeve length ( $L_0 = 3 \, \text{mm}$ ), Eq. A.1 can be written as

$$\frac{\Delta P}{P_0} + \frac{10}{3}\varepsilon = \frac{\Delta T}{T_0},\tag{A.2}$$

where the change of pressure can be considered as

$$\Delta P = \frac{F}{A} = \frac{k}{A} \Delta \delta,\tag{A.3}$$

where F is the normal force due to the increase of pressure exerted on the end face of the fibre and the area of the disc inside the cavity, and k is the stiffness of the sensor with respect to the force F.

By using Eqs. A.3 and 5, Eq. A.2 can be simplified as

$$\frac{1}{A/k} \frac{L_0}{3P_0} \varepsilon + \frac{10}{3} \varepsilon = \frac{\Delta T}{T_0} . \tag{A.4}$$

To further simplify Eq. A.4, one needs to find the value of k/A in the FEM model. The FEM model is the same as the one used for the above-mentioned thermal expansion analysis, expect that no temperature change is applied and an outward pressure of 1 Pa is applied on both sides of the sensor cavity, i.e., on the fibre and on the area of the disc inside the cavity. Fig. A.2 shows the contour of displacement under the applied pressure. The change of fibre-disc distance is  $6.7 \times 10^{-8}$  mm where its value can be considered as the value of A/k (mm/Pa), knowing the pressure is 1 Pa.

Therefore, Eq. A.4 becomes,

$$\varepsilon = 0.0066 \frac{\Delta T}{T_0},\tag{A.5}$$

where the sensor strain caused by the change of air pressure induced by the temperature change can be calculated. For a temperature increase of  $\Delta T$  = 60 K, the sensor strain is 0.14% according to Eq. A.5.

**Total temperature effects on the sensor deformation.** The total strain caused by the temperature change can be obtained by adding strains calculated from the thermal expansion and the increase of air pressure which for a 60 °C increase of temperature is 0.52%. This deformation is much smaller than the strain (20%) measured in the banana drying experiments described in the main text.

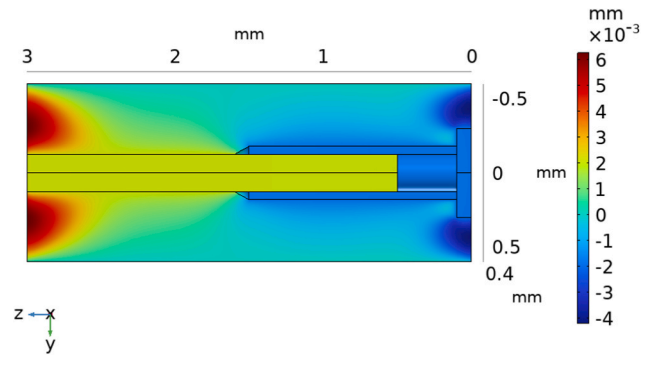


Fig. A.1. The contour of displacement caused by thermal expansion of the sensor under the temperature increase of 60 °C.

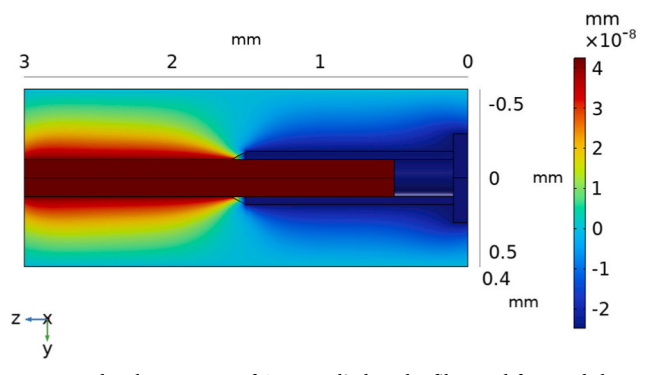


Fig. A.2. The contour of displacement under the pressure of 1 Pa applied to the fibre end face and the area of the disc inside the cavity.

#### References

Akiyama, T., Liu, H., & Hayakawa, K.-I. (1997). Hygrostress-multicrack formation and propagation in cylindrical viscoelastic food undergoing heat and moisture transfer processes. *International Journal of Heat and Mass Transfer*, 40(7), 1601–1609. https://doi.org/10.1016/S0017-9310(96)00206-2

Aprajeeta, J., Gopirajah, R., & Anandharamakrishnan, C. (2015). Shrinkage and porosity effects on heat and mass transfer during potato drying. *Journal of Food Engineering*, 144, 119–128. https://doi.org/10.1016/j.jfoodeng.2014.08.004

Deng, L., & Cai, C. (2007). Applications of fiber optic sensors in civil engineering Structural Engineering & Mechanics, 25(5), 577–596. Erik, A. M., Michael, D. T., & Anthony, D. P. (2011). Experimental verification of a model describing the intensity distribution from a single mode optical fibre. Smart Sensor Phenomena, Technology, Networks, and Systems 7982 (Vol. 2011). SPIE.

Gulati, T., & Datta, A. K. (2015). Mechanistic understanding of case-hardening and texture development during drying of food materials. *Journal of Food Engineering*, 166, 119–138. https://doi.org/10.1016/j.jfoodeng.2015.05.031

Higson, G. R. (1964). Recent advances in strain gauges. Journal of Scientific Instruments, 41(7), 405. https://doi.org/10.1088/0950-7671/41/7/301

Krokida, M., & Maroulis, Z. (2000). Quality changes during drying of food materials. Drying Technology in Agriculture and Food sciences, 4(2), 61–68.

Lagakos, N., Bucaro, J. A., & Jarzynski, J. (2010). Intensity modulated fiber optic strain sensor. U.S. Patent No., 7, 646–946, 12 Jan. 2010.

- Liu, T., Wu, M., Rao, Y., Jackson, D. A., & Fernando, G. F. (1998). A multiplexed optical fibre-based extrinsic Fabry-Perot sensor system for in-situ strain monitoring in composites. Smart Materials and Structures, 7(4), 550.
- Macedo, L. L., Wallaf, C. V., Cintia, da S. A., Sérgio, H. S., & Luciano, J. Q. T. (2020). Effect of drying air temperature on drying kinetics and physicochemical characteristics of dried banana. *Journal of Food Process Engineering*, 43(9), Article e13451. https://doi.org/10.1111/jfpe.13451
- Madiouli, J., Sghaier, J., Orteu, J.-J., Robert, L., Lecomte, D., & Sammouda, H. (2011). Non-contact Measurement of the shrinkage and calculation of porosity during the drying of banana. *Drying Technology*, 29(12), 1358–1364. https://doi.org/10.1080/ 07373937.2011.561460
- Mahiuddin, M., Khan, M. I. H., Kumar, C., Rahman, M. M., & Karim, M. A. (2018). Shrinkage of food materials during drying: Current status and challenges. Comprehensive Reviews in Food Science and Food Safety, 17(5), 1113–1126. https://doi.org/10.1111/1541-4337.12375
- Merzbacher, C. I., Kersey, A. D., & Friebele, E. J. (1996). Fiber optic sensors in concrete structures: A review. Smart Materials and Structures, 5(2), 196–208. https://doi.org/ 10.1088/0964-1726/5/2/008
- Montazerian, H., Rashidi, A., Milani, A. S., & Hoorfar, M. (2020). Integrated sensors in advanced composites: A critical review. *Critical Reviews in Solid State and Materials Sciences*, 45(3), 187–238. https://doi.org/10.1080/10408436.2019.1588705
- Murphy, K. A., Gunther, M. F., Vengsarkar, A. M., & Claus, R. O. (1992). Fabry–Perot fiber-optic sensors in full-scale fatigue testing on an F-15 aircraft. *Applied Optics*, 31 (4), 431–433. https://doi.org/10.1364/AO.31.000431
- Ozturk, O. K., & Takhar, P. S. (2020). Hybrid mixture theory-based modeling of moisture transport coupled with quality changes in strawberries and carrots. *Drying Technology*, 1–18. https://doi.org/10.1080/07373937.2020.1733005
- Ozturk, O. K., & Takhar, P. S. (2020). Physical and viscoelastic properties of carrots during drying. *Journal of Texture Studies*, 51(3), 532–541. https://doi.org/10.1111/ itxs.12496

- Siegman, A. E. (1986). Lasers: University science books. Mill Valley, CA, 37(208), 169.
   Silva, V., Costa, J. J., Figueiredo, A. R., Nunes, J., Nunes, C., Ribeiro, T. I. B., et al. (2016). Study of three-stage intermittent drying of pears considering shrinkage and
- (2016). Study of three-stage intermittent drying of pears considering shrinkage and variable diffusion coefficient. *Journal of Food Engineering*, 180, 77–86. https://doi.org/10.1016/j.jfoodeng.2016.02.013
- Sturm, B., Nunez Vega, A.-M., & Hofacker, W. C. (2014). Influence of process control strategies on drying kinetics, colour and shrinkage of air dried apples. *Applied Thermal Engineering*, 62(2), 455–460. https://doi.org/10.1016/j. applthermaleng.2013.09.056
- Takhar, P. S. (2011). Hybrid mixture theory based moisture transport and stress development in corn kernels during drying: Coupled fluid transport and stress equations. *Journal of Food Engineering*, 105(4), 663–670. https://doi.org/10.1016/j. jfoodeng.2011.03.033
- Takhar, P. S. (2014). Unsaturated fluid transport in swelling poroviscoelastic biopolymers. Chemical Engineering Science, 109, 98–110.
- Takhar, P. S., Maier, D. E., Campanella, O. H., & Chen, G. (2011). Hybrid mixture theory based moisture transport and stress development in corn kernels during drying: Validation and simulation results. *Journal of Food Engineering*, 106(4), 275–282. https://doi.org/10.1016/j.jfoodeng.2011.05.006
- Window, A. L. (1992). Strain gauge technology. Netherlands: Springer.
- Yadollahinia, A., Latifi, A., & Mahdavi, R. (2009). New method for determination of potato slice shrinkage during drying. Computers and Electronics in Agriculture, 65(2), 268–274. https://doi.org/10.1016/j.compag.2008.11.003
- Yuan, Y., Tan, L., Xu, Y., Yuan, Y., & Dong, J. (2019). Numerical and experimental study on drying shrinkage-deformation of apple slices during process of heat-mass transfer. *International Journal of Thermal Sciences*, 136, 539–548. https://doi.org/10.1016/j. iithermalsci.2018.10.042
- Zheng, J., & Albin, S. (1999). Self-referenced reflective intensity modulated fiber optic displacement sensor. *Optical Engineering*, 38, 227–232. https://doi.org/10.1117/ 1.602260